Univerzita Karlova v Praze
Matematicko-fyzikální fakulta

BAKALÁŘSKÁ PRÁCE

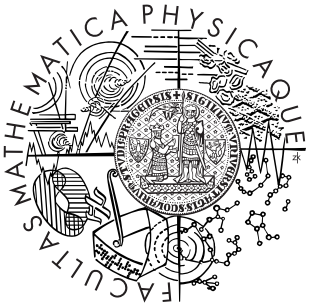

Jozef Veselý

Mikrostrukturní změny v tenkých kovových fóliích

Katedra fyziky kovů

Vedoucí bakalářské práce: Doc. RNDr. Miroslav Cieslar, CSc.
Studijní program: fyzika, obecná fyzika

2006

Chcel by som poďakovať vedúcemu práce doc. Cieslarovi za to, že mi ukázal elektronový mikroskop a za neuveritelnú trpezlivosť.

Prohlašuji, že jsem svou bakalářskou práci napsal samostatně a výhradně s použitím citovaných pramenů. Souhlasím se zapůjčováním práce a jejím zveřejňováním.

V Praze dne 10. srpna 2006 Jozef Veselý

Contents

Název práce: Mikrostrukturní změny v tenkých kovových fóliích
Autor: Jozef Vesely
Katedra (ústav): Katedra fyziky kovů
Vedoucí bakalářské práce: Doc. RNDr. Miroslav Cieslar, CSc.
e-mail vedoucího: cieslar@met.mff.cuni.cz

Abstrakt: Príprava tenkých fólií plynulým liatím medzi valce, je výhodná pretože skracuje výrobný cyklus. Matrica je vysoko presýtená, kvoli velkým rýchlostiam tuhnutia. Táto práca sa zaoberá mikroštruktúrnymi a fázovými zmenami nastávajúcimi v zliatinách na báze Al-Fe-Mn-Si pri žíhaní. Štyri zliatiny s mierne odlišným zložením boli študované pomocou TEM a meraní elektrickej rezistivity. Zistili sme, že rezistivita je ovplyvnená najmä precipitáciou nových častíc, obohacovaním existujúcich častíc o prímesi rozpustené v matrici a transformáciami primárnych fází. V zliatinách bohatých na Si bola pozorovaná iba fáza α-$Al_{15}(Mn,Fe)_3Si_2$, zatial čo v zliatine s nízkym obsahom Si prebehla transformácia z fáze α-Al_8Fe_2Si cez α-$Al_{15}(Mn,Fe)_3Si_2$ až na $Al_6(Mn,Fe)$.

Klíčová slova: plynulé liatie medzi valce, zliatina na báze Al-Fe-Mn-Si, rekryštalizácia, fázové zmeny

Title: Microstructural changes in thin metallic foils
Author: Jozef Veselý
Department: Department of Metal Physics
Supervisor: Doc. RNDr. Miroslav Cieslar, CSc.
Supervisor's e-mail address: cieslar@met.mff.cuni.cz

Abstract: Use of the twin-roll casting for preparation of thin foils is advantageous because it shortens the production cycle. Matrix is highly supersaturated due to the high solidification rates. In this work microstructure and phase transformations in Al-Fe-Mn-Si-based alloys during annealing were studied. Four alloys of slightly varied composition were studied by means of TEM and resistivity measurements. It was found that resistivity is influenced mostly by precipitation of new particles, enrichment of existing particles by solutes from matrix and transformations of primary phases. In Si rich alloys only α-$Al_{15}(Mn,Fe)_3Si_2$ phase was observed, while in alloy with low Si content transformation from α-Al_8Fe_2Si throung α-$Al_{15}(Mn,Fe)_3Si_2$ into $Al_6(Mn,Fe)$ phase occured.

Keywords: twin-roll casting, Al-Fe-Mn-Si-based alloy, recrystallization, phase transformations

1 Introduction

Thin foils from aluminium alloys are used in the heat exchangers in car industry. Thin foils are traditionally obtained by hot and cold rolling of thick ingot plates obtained by direct chill (DC) casting. The twin-roll casting (TRC) significantly shortens the production cycle and reduces the energy needs. The molten material solidifies directly between two rolls and a few millimeter thick strip is produced. The strip is then cold rolled to final thickness.

During the TRC high solidification rates are achieved, resulting into a much higher saturation of the solid solution. Consequently the knowledge of physical metallurgical behaviour of the DC cast alloys can not be applied. The TRC aluminium alloys are therefore subject of an intense research [1, 2, 3].

In this work the influence of small variations in the alloy composition on the microstructure, and phase transformations during the annealing is studied by the means of transmission electron microscopy (TEM).

2 Experimental details

2.1 Material origin

Four Al-Fe-Mn-Si-based alloys of a slightly varied composition (tab. 2.1) were supplied by AIB a.s.. The material was prepared by a continuous twin-roll casting into 8 mm thick strips that were further (cold) rolled into 5 mm.

The LV, HV and S alloys had nearly the same Si/Mn ratio but different content of Mn. The S and Z had approximately the same Mn content but the Z alloy had considerably lower Si/Mn ratio.

Designation	Al	Mn	Si	Fe	Cu	Si/Mn ratio
AW-3003 [4]	remainder	$1.0 - 1.5$	< 0.6	< 0.7	$0.05 - 0.20$	
HV	remainder	1.31	0.75	0.59	0.13	0.57
LV	remainder	1.02	0.59	0.48	0.11	0.58
S	remainder	0.90	0.50	0.53	0.17	0.56
Z	remainder	0.86	0.10	0.61	0.16	0.12

Table 2.1: Composition of studied materials (in wt. %).

2.2 Experimental methods

All materials were subjected to the resistometry analysis in the work of Slamová et. al [3]. Electrical resistivity was measured during linear heating up to 620 °C at the rate of 1 K/min. A main feature on normalized differential resistivity $\frac{1}{R}\frac{\mathrm{d}R}{\mathrm{d}T}$ curves (fig. 2.1) is the valley around 400 °C.

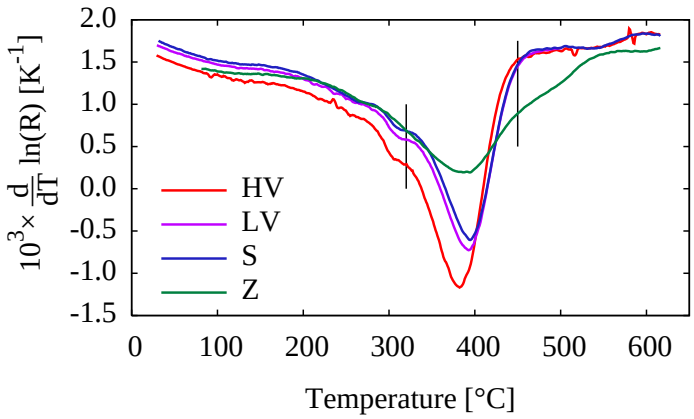

Figure 2.1: Temperature dependence of normalized differential resistivity for all four materials. Vertical lines mark temperatures of TEM observations.

The valley on the curve from alloy with low Si content (Z) is much shallower and flatter when compared to the deep and narrow valleys on the other curves. The curves from alloys with high Si content (HV, LV and S) exhibit a slight "bump" around 320 °C.

In addition to the initial and final state, two temperatures around the valley — 320 and 450 °C — were chosen for TEM observations. TEM observations are expected to explain the phenomenons behind these excessive resistivity changes.

The TEM observations were performed using the JEOL JEM 2000FX transmission electron microscope operating at 200 kV, equipped with an energy dispersive X-ray (EDX) analyser LINK AN 10000. A double tilt specimen holder was used. The Cu peak appearing in the EDX spectra is due to the holder and shall not be taken into account.

2.3 Specimen preparation

Cylinders 3 mm in diameter were cut from received material by a spark-machine (fig. 2.2). The DSC device was used to anneal samples to specified temperatures under the same heating rate as the resistivity measurement — 1 K/min.

The samples were further grinded to the thickness of 0.1 mm and then electropolished under 15 V at −15 °C in 33 % solution of nitric acid in methyl alcohol, to prepare the TEM specimens.

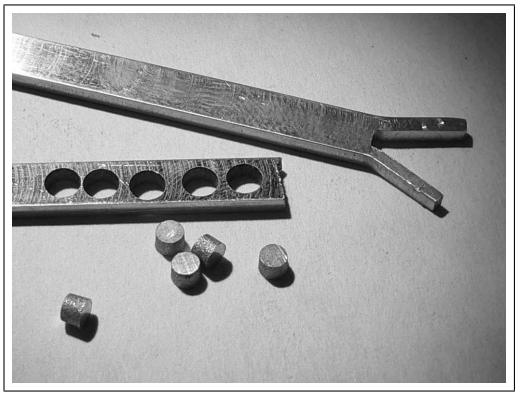

Figure 2.2: Received sample (with contacts for 4-point resistivity measurement) and cylinders cut by spark-machine.

3 Experimental results

3.1 TEM observations

3.1.1 Initial state

An initial state of all alloys can be characterized by high dislocation density (fig. 3.1). The dislocations were introduced in the material by deformation during the cold rolling stage. Another result of rolling is the elongated shape of the grains (fig. 3.2). Their length was several microns along the rolling direction and width about one micron.

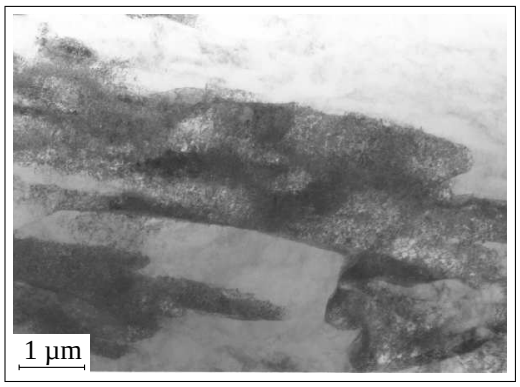

Figure 3.1: High dislocation density is main feature of initial states, S alloy.

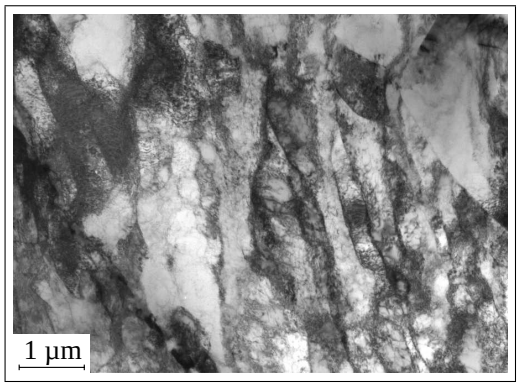

Figure 3.2: Subgrains prolonged in the rolling direction, Z alloy.

Rare areas where the recovery had already started could be found in all alloys (fig. 3.3). The density of dislocations was reduced and a cell substructure began to form. A partially recovered substructure could be found mostly in the vicinity of the particles of the primary phases (fig. 3.4).

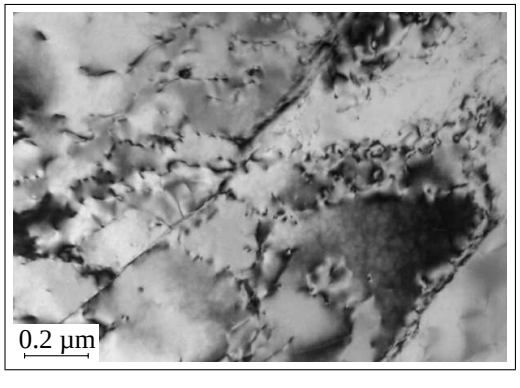

Figure 3.3: Recovered cells, LV alloy.

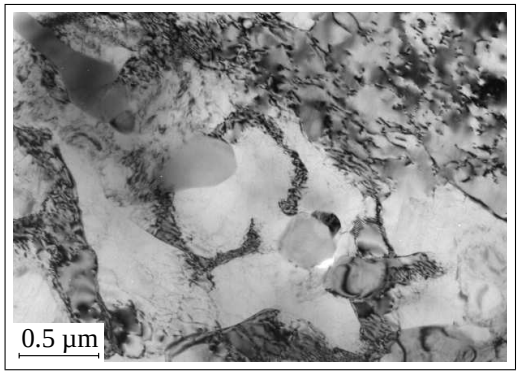

Figure 3.4: Partially recovered cell structure near particles of primary phases, Z alloy.

Particles of primary phases were formed by the eutectic reaction during rapid cooling of the molten material. They form either dendritic colonies (fig. 3.5) or "chains" along grain boundaries (fig. 3.6).

The analysis of the SAD patterns (section 3.2) showed that in alloys with high Si content (HV, LV and S) both kinds of particles have a cubic α-$Al_{15}(Mn, Fe)_3Si_2$ structure. The analyzed particles in the Z alloy (low Si content) have a hexagonal α-Al_8Fe_2Si structure.

Figure 3.5: Dendritic colony of primary phase, HV alloy.

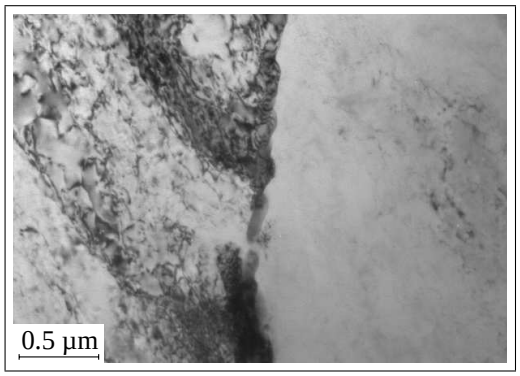

Figure 3.6: Primary phases particles along grain boundary, HV alloy.

3.1.2 Annealing up to 320 °C

After the annealing up to 320 °C, the recovery process in all alloys is in its full strength. Almost everywhere dislocations cease in numbers and gather to form boundaries of the cell substructure (fig. 3.7). Near the particles of the primary phases, where the recovery had originally started, recrystallization nuclei and grains were found in this state (fig. 3.8).

The morphology of the particles did not change. The grains elongated in the rolling direction can still be recognized.

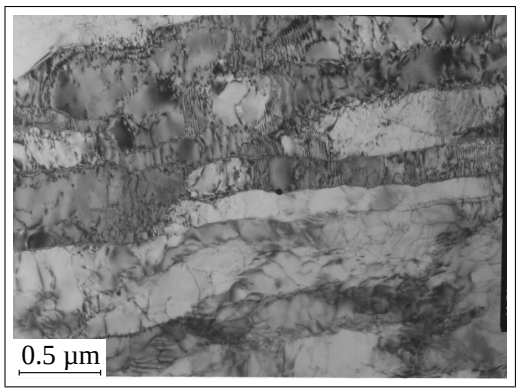

Figure 3.7: Recovery in progress, HV alloy.

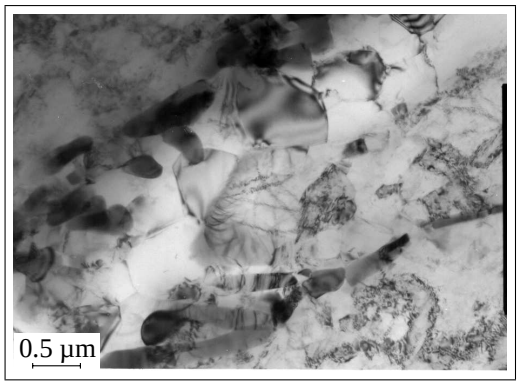

Figure 3.8: Recrystallized grains near particles of primary phase, HV alloy.

New particles rich in Si appeared in the LV alloy (fig. 3.9). Occasional rectangular Si rich particles were found also in the S and Z alloys (fig. 3.10). Analysis of the SAD patterns revealed that these particles have cubic structure of pure Si. The Si content was confirmed by EDX (fig. 3.11).

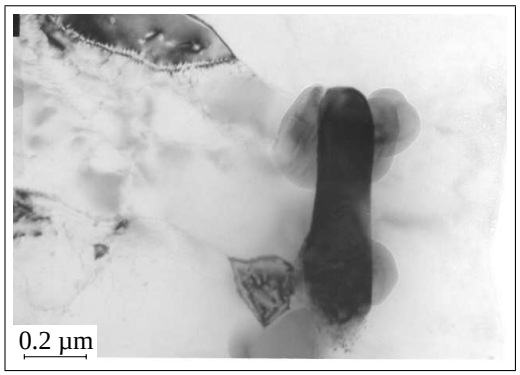

Figure 3.9: Dark α-$Al_{15}(Mn,Fe)_3Si_2$ particle surrounded by lighter Si particles in LV alloy.

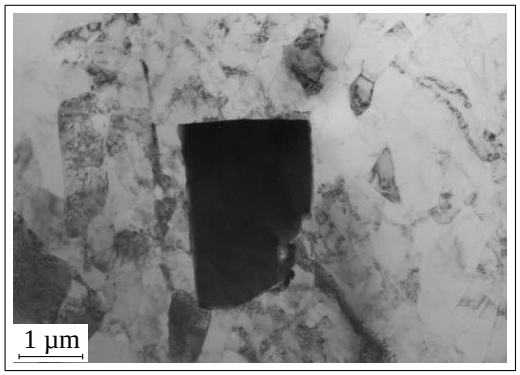

Figure 3.10: Angular Si particle in Z alloy.

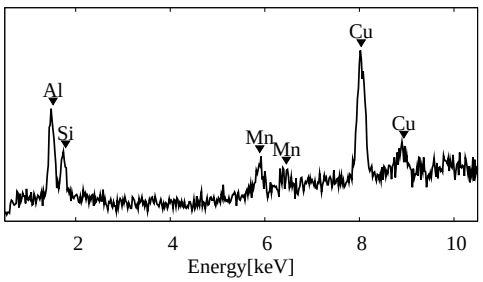

Figure 3.11: EDX spectrum form Si particle on figure 3.10.

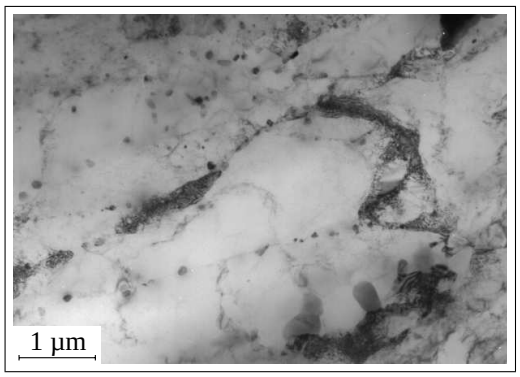

Figure 3.12: Precipitates on grain boundaries in S alloy.

In the Z alloy the particles with originally hexagonal α-Al_8Fe_2Si structure transformed to cubic α-$Al_{15}(Mn,Fe)_3Si_2$.

In the S alloy new tiny 0.1 µm precipitates appeared on the subgrain boundaries (fig. 3.12).

3.1.3 Annealing up to 450 °C

After the annealing up to 450 °C new precipitates can be found in all alloys. In the LV and HV materials the precipitates are evenly distributed in the matrix (fig 3.13). In the S alloy the precipitates observed at 320 °C on the subrain boundaries became coarser, furthermore some fine precipitates appeared in the matrix (fig. 3.15). In the Z alloy precipitates were found mostly on the subgrain boundaries, very few of them were present in the matrix (fig. 3.17).

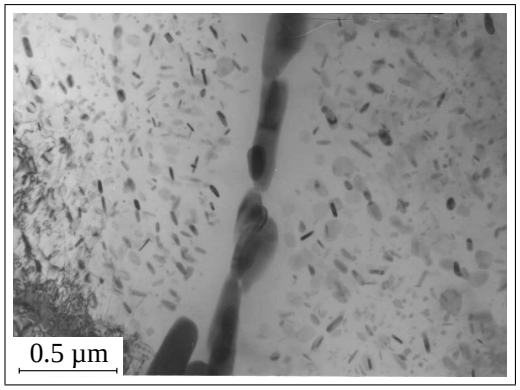

Figure 3.13: PFZ near primary particles, but otherwise evenly distributed precipitates in HV alloy.

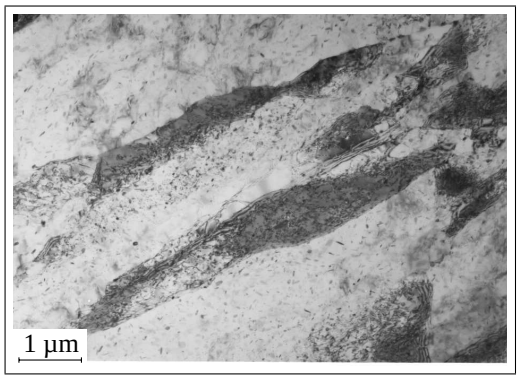

Figure 3.14: Partially recovered substructure, LV alloy.

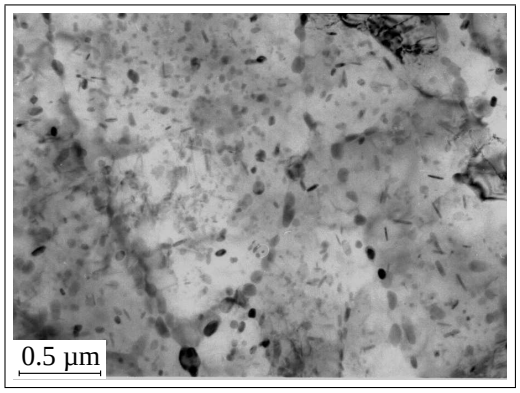

Figure 3.15: Fine precipitates in the matrix and coarser on (former) subgrain boundaries, S alloy.

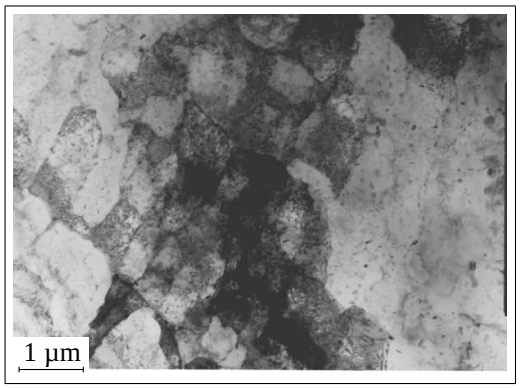

Figure 3.16: Polygonized substructure, S alloy.

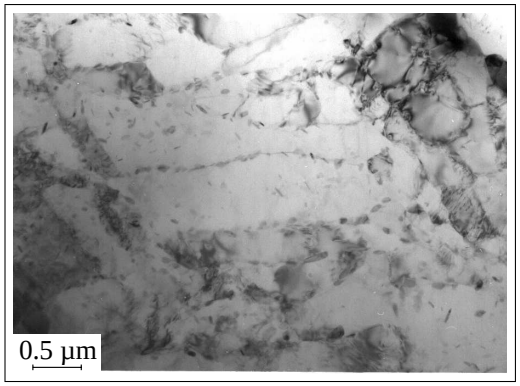

Figure 3.17: Precipitates in Z alloy formed mostly on subgrain boundaries.

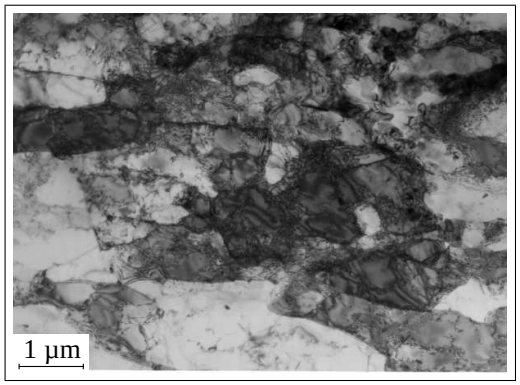

Figure 3.18: Polygonized substructure, Z alloy.

The precipitates interact with moving dislocations and thus affect ongoing recovery and recrystallization. In the LV and HV alloys elongated subgrains are only partially recovered with a large number of small cells (fig. 3.14). However, in the S and Z alloys the polygonized substructures are more distinct (fig. 3.16 and 3.18).

In all alloys no precipitates appear near the primary particles. Precipitation free zones (fig. 3.13) and even whole grains without precipitates (fig. 3.19) were observed in the neighbourhood of the primary particles. The EDX showed that such grains contain almost pure Al with very low content of dissolved Mn (fig. 3.20).

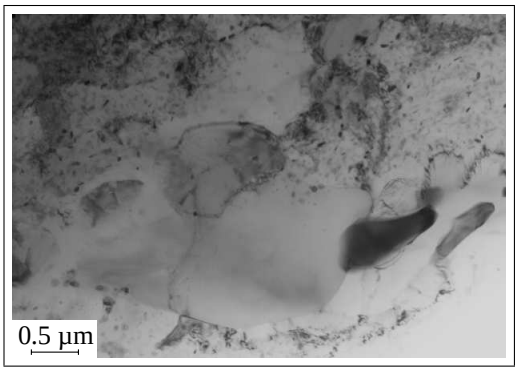

Figure 3.19: Recrystallized grain near primary particle containing no precipitates.

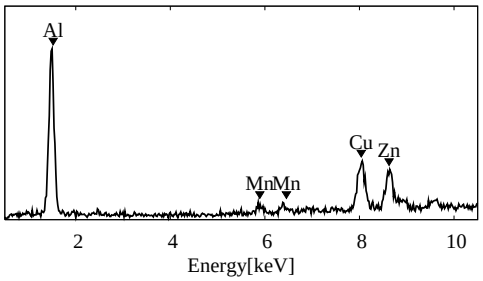

Figure 3.20: EDX spectrum form recrystallized grain on figure 3.19.

3.1.4 Final state, annealing up to 620 °C

After the annealing up to the final temperature 620 °C fully recrystallized structure can be observed in all alloy. A homogeneous matrix or very huge grains were observed.

All precipitates and particles became coarser. The HV alloy constains the largest number of the precipitates distributed in the matrix (fig. 3.21). Much less precipitates were found in the alloys with lower content of additions (fig. 3.22). In the low Si content alloy (Z) precipitates were found only along the former subgrain boundaries (fig. 3.23).

The SAD analysis showed that all analysed particles and precipitates in the Z sample had an orthorhombic $Al_6(Mn, Fe)$ structure. All structures in the other alloys were cubic α-$Al_{15}(Mn, Fe)_3Si_2$.

The EDX analysis showed that the Mn content in primary particles increased both in the high and low Si content alloys S and Z respectively (fig. 3.25 and 3.26). All analysed precipitates (also at 450 °C) contained more Mn than one in particles (fig. 3.24).

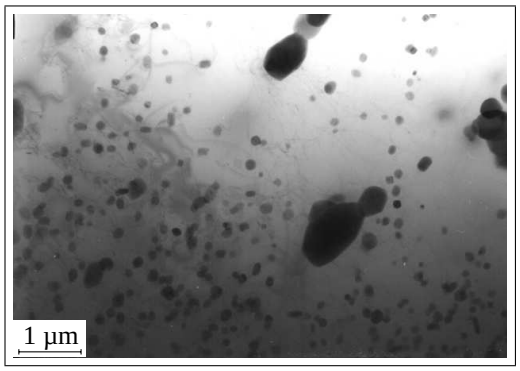

Figure 3.21: Final state HV alloy.

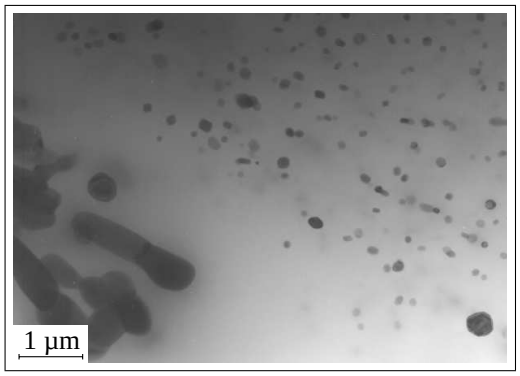

Figure 3.22: Final state S alloy.

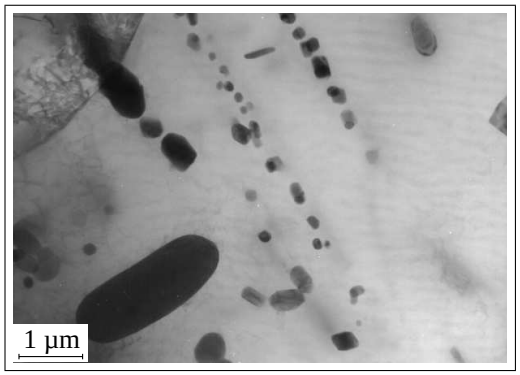

Figure 3.23: Final state Z alloy.

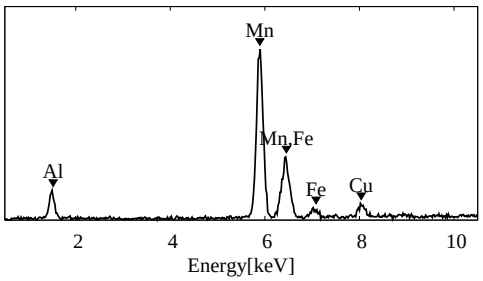

Figure 3.24: EDX spectrum from precipitate, S alloy final state.

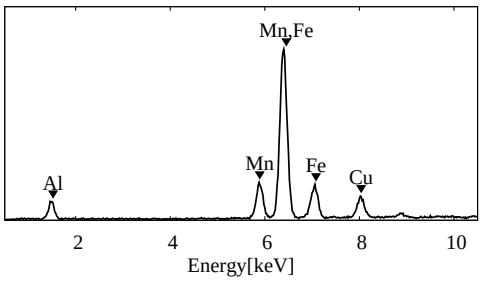

Figure 3.25: EDX spectrum from primary particle, Z alloy annealed up to 450 °C.

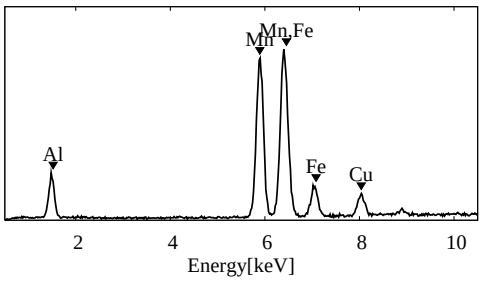

Figure 3.26: EDX spectrum from primary particle, Z alloy final state.

3.2 SAD analysis

3.2.1 Software

A computer programme was written to help with diffraction pattern analysis. Firstly the diffraction pattern needs to be digitized. An ordinary scanner is adequate for this purpose.

After loading the image file, bright spots are located. Various image processing methods were tried. Very good results are achieved if the image is firstly gaussian averaged to suppress noise. The sharp local maxima then corespond to the bright spots. The width of the gaussian should match the size of the spots we want to detect (small spots can be averaged away by wide gaussian).

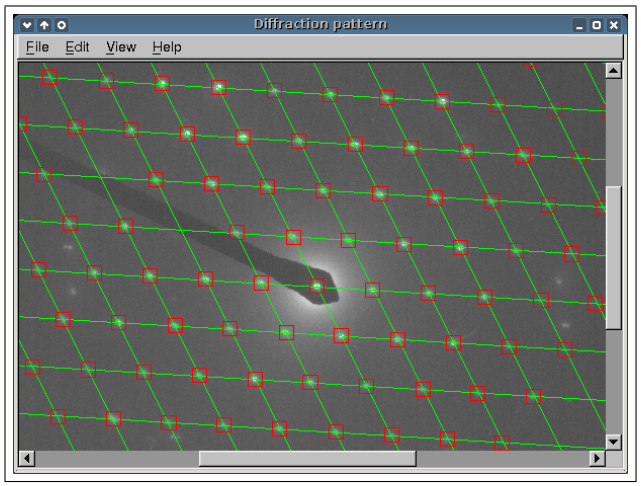

Figure 3.27: Main window — scanned diffraction pattern overlayed by selected spots and best fit grid.

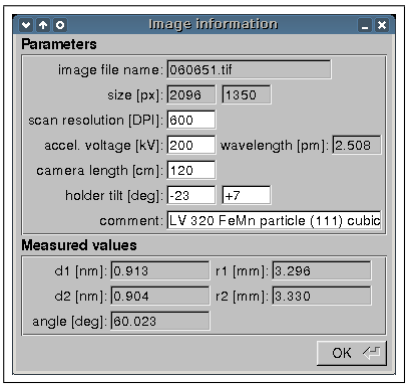

Figure 3.28: Parameters of image along with measured distances and angle.

When bright spots are found it is up to the user to select those which form regular pattern. Regular grid is automatically fitted (the least squares) to the selected spots (fig. 3.27).

When the scan resolution (DPI), the acceleration voltage, and the camera length L are supplied, the distance between the lattice planes in the crystal d_{hkl} is calculated (fig. 3.28) from Bragg equation [5] (r_{hkl} is distance measured on film)

$$d_{hkl} = \frac{\lambda}{2\sin\theta} \approx \frac{\lambda L}{r_{hkl}} \tag{3.1}$$

This programme offers several advantages over traditional "lens and ruler" method: The measurement is more precise, since much more spots are considered. The weak spots invisible to human eye can be detected. Poor diffraction patterns can be measured, as overlayed grid helps to decide which spots belong to the pattern (even doubly exposed images could be measured). The measurement can be saved together with the information about the diffraction pattern for further processing.

The programme runs on both Windows and Linux, and it is available on the attached CD-ROM, as well as on `http://jove.matfyz.cz/diffract/`.

3.2.2 Analysis of diffraction patterns

For every analysed particle usually three diffraction patterns from different crystall zone axes were taken. The precipitates were mostly too small to find more low index zone axes, therefore the patterns from several precipitates were taken.

Designation	Type	a [nm]	b [nm]	c [nm]
Al	cubic	0.405	-	-
Si	cubic	0.543	-	-
α-$Al_{15}(Mn,Fe)_3Si_2$	cubic	1.26	-	-
α-Al_8Fe_2Si	hexa	1.23	-	26.3
$Al_6(Mn,Fe)$	ortho	0.65	0.75	0.88

Table 3.1: Crystallographic structure of encountered phases.

The diffraction patterns were measured using the software described above. The resulting d_{hkl} distances and angles were matched with the interplanar distances and angles calculated for crystallographic phases that are known to appear in Al-Mn-Fe-based alloys (tab. 3.1) [6, 7]. Special care was taken to match and align the crystallographic directions of the zone axes with the experimental tilts recorded for each pattern.

	Specimen	Temperature	Structure
Si particles	LV, S	320 °C	cubic Si
particles	HV, LV, S	all	cubic α-$Al_{15}(Mn,Fe)_3Si_2$
precipitates	HV, LV, S	450, 620 °C	cubic α-$Al_{15}(Mn,Fe)_3Si_2$
particles	Z	initial	hexa α-Al_8Fe_2Si
particles	Z	320, 450 °C	cubic α-$Al_{15}(Mn,Fe)_3Si_2$
particles	Z	620 °C	ortho $Al_6(Mn,Fe)$
precipitates	Z	450 °C	cubic α-$Al_{15}(Mn,Fe)_3Si_2$
precipitates	Z	620 °C	ortho $Al_6(Mn,Fe)$

Table 3.2: Summary of structures determined from SAD patterns.

As much as 25 structures were analysed. The results are summarized in the table 3.2. The examples of each kind of structure are in the figures 3.29 to 3.32. These figures include diffraction patterns, stereographic projection of oriented crystall with experimental tilts marked by crosses, and a table with measured and calculated d_{hkl} distances.

During the analysis only the point groups of lattices were taken into account, no attempt was made to determine the space group from forbidden reflections. However, it can be seen from the figure 3.33 that forbidden reflections varied in various phases classified as cubic α-$Al_{15}(Mn,Fe)_3Si_2$. These differences are due to the different stoichiometry of the phases.

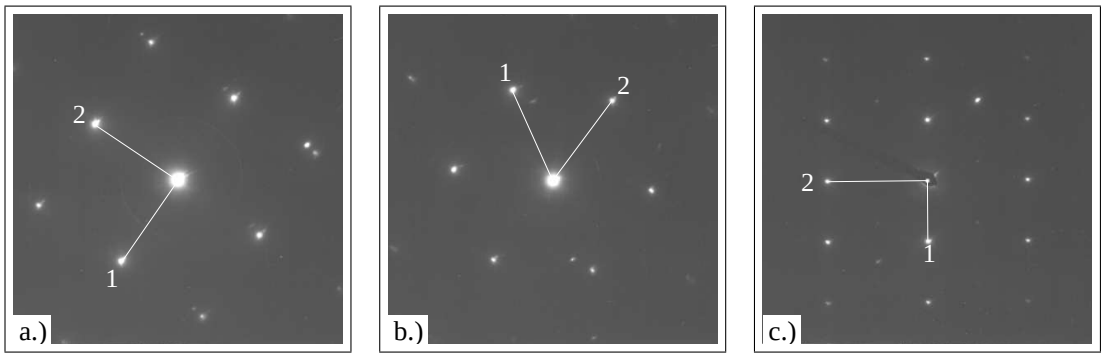

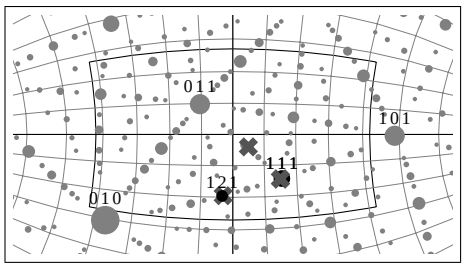

Pattern	d_1	d_2	α	$\vec{g}_1$	$\vec{g}_2$	zone
a.)	0.197	0.196	89.2	$2\bar{2}0$	220	001[a]
	0.192	0.192	90			
b.)	0.197	0.197	60.8	$2\bar{2}0$	$02\bar{2}$	111
	0.192	0.192	60			
c.)	0.322	0.195	89.8	$1\bar{1}1$	$20\bar{2}$	121
	0.314	0.192	90			

[a] Most probably from other grain of the same particle, because measured tilts do not match.

d_1 and d_2 in nm, α in degrees, calculated values are in second row.

Figure 3.29: Analysis of SAD patterns of from Si particle. LV alloy quenched from 320 °C.

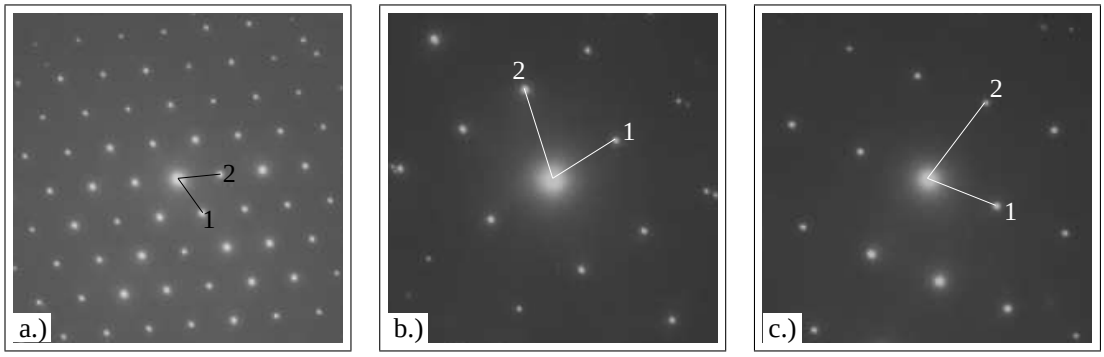

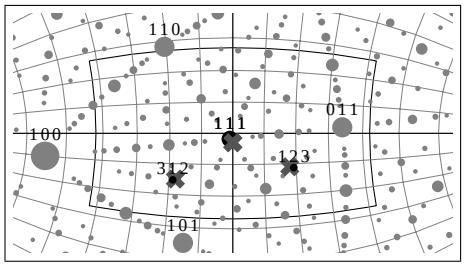

Pattern	d_1	d_2	α	$\vec{g}_1$	$\vec{g}_2$	zone
a.)	0.919	0.911	59.9	$10\bar{1}$	$01\bar{1}$	111
	0.891	0.891	60			
b.)	0.528	0.413	75.4	$1\bar{2}1$	$30\bar{1}$	123
	0.514	0.398	75			
c.)	0.531	0.411	74.5	$11\bar{2}$	$\bar{1}30$	312
	0.514	0.398	75			

d_1 and d_2 in nm, α in degrees, calculated values are in second row.

Figure 3.30: Analysis of SAD patterns from α-$Al_{15}(Mn, Fe)_3Si_2$ particle. Final state of S alloy.

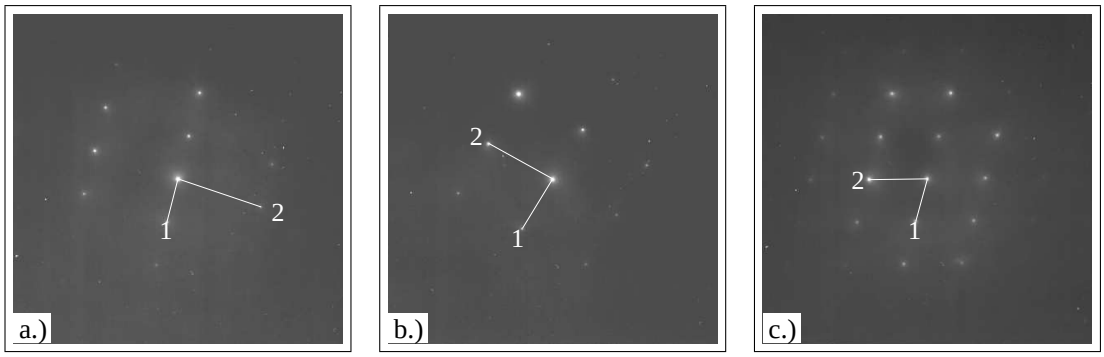

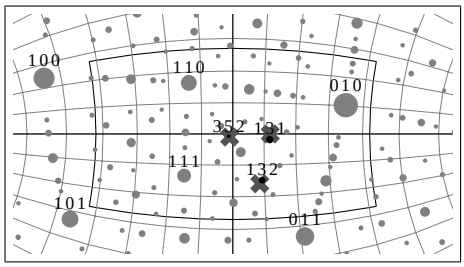

Pattern	d_1	d_2	α	$\vec{g}_1$	$\vec{g}_2$	zone
a.)	0.441	0.222	85.7	$\bar{1}1\bar{1}$	$\bar{2}03$	352
	0.429	0.218	85.4			
b.)	0.336	0.267	87.6	$\bar{1}1\bar{2}$	$\bar{2}02$	131
	0.328	0.261	87.9			
c.)	0.441	0.335	73.9	$\bar{1}1\bar{1}$	$\bar{1}\bar{1}2$	132
	0.429	0.328	73.7			

d_1 and d_2 in nm, α in degrees, calculated values are in second row.

Figure 3.31: Analysis of SAD patterns from orthorhombic $Al_6(Mn, Fe)$ particle. Final state of Z alloy.

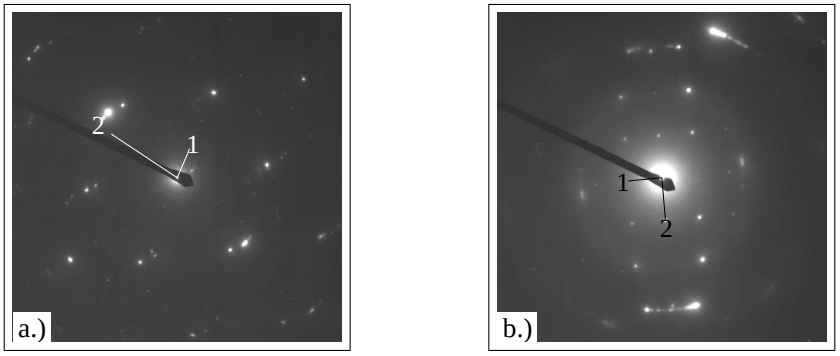

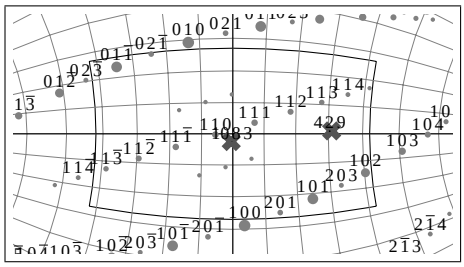

Pattern	d_1	d_2	α	$\vec{g}_1$	$\vec{g}_2$	zone
a.)	0.632	0.246	79.8	$\bar{1}2.0$	$\bar{5}1.2$	429
	0.615	0.229	79.3			
b.)	0.578	0.461	89.4	$2\bar{1}.2$	$2\bar{1}.\bar{4}$	10 8 3
	0.557	0.449	87.6			

d_1 and d_2 in nm, α in degrees, calculated values are in second row.

Figure 3.32: Analysis of SAD patterns from hexagonal α-Al_8Fe_2Si particle. Initial state of Z alloy.

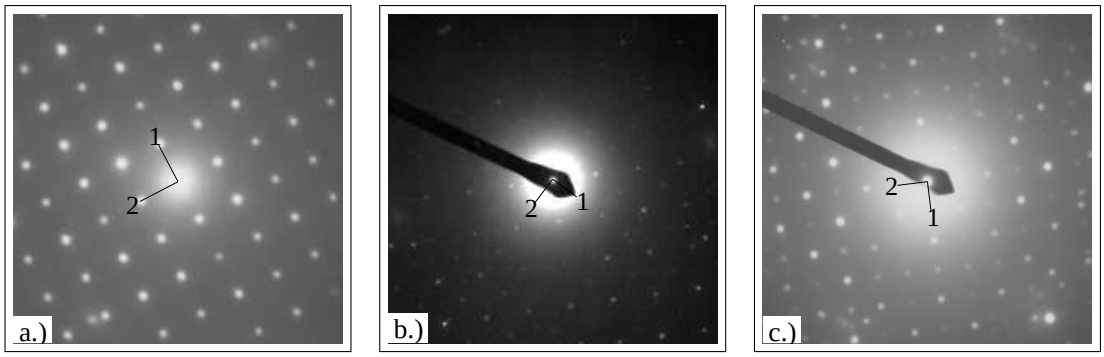

Figure 3.33: Cubic 001 zone with 100 type reflections a.) forbidden — particle S 450 °C; b.) weak — precipitate S 450 °C; c.) allowed — precipitate HV 450 °C.

4 Discusion

The rapid cooling of the twin-roll cast material is responsible for the high content of Mn and Si dissolved in the matrix (supersaturated solid solution).

In the initial state particles of the cubic α-$Al_{15}(Mn, Fe)_3Si_2$ phase were present in alloys with high Si content (HV, LV and S). In the Z alloy particles of the metastable hexagonal α-Al_8Fe_2Si phase were formed due to the low Si content. During annealing up to 320 °C mobility of Si dissolved in the matrix increased and these metastable phases transformed into cubic α-$Al_{15}(Mn, Fe)_3Si_2$.

The recovery of the deformed structure was observed after the annealing up to the 320 °C. The dislocations alone do not have strong influence on the electrical resistivity, but atoms of solutes freed by the recovery of dislocations could be responsible for presence the "bump" on the resistivity curve around 320 °C [3].

The resistivity depends mostly on the amount of solutes dissolved in the matrix [7]. The formation of precipitates from solutes dissolved in the matrix is the cause of the deep valleys on the resistivity curves. The depth of the valley is correlated with the amount of precipitates.

Only the small number of precipitates was observed in the Z alloy. Moreover the valley on the Z resistivity curve is broader than the range in which precipitates appeared (between 320 and 450 °C). This suggests that enrichment of primary particles and their coarsening contribute significantly to resistivity changes.

Primary particles are enriched by the solutes in the nearby matrix in all alloys but the precipitation has usually stronger influence on the resistivity. The precipitation free zones are the proof of the depletion of the matrix near primary particles. The enrichment of primary particles was confirmed also by the EDX analysis.

At 320 °C first recrystallized grains were observed in the neighbourhood of the particles. Recovery and recrystallization start near the primary particles because dislocations are not hindered by sollutes in the depleted matrix and because of the higher amount of deformation energy that was stored near the particles (particle stimulated nucleation) [2, 6].

The low Si content in the Z alloy is not enough to sustain cubic α-$Al_{15}(Mn, Fe)_3Si_2$ structure, therefore the transformation to orthorhombic $Al_6(Mn, Fe)$ occurs between 450 and 620 °C. During this transformation even more Mn is taken from the matrix. This can explain "bumps" in the corresponding part of Z resistivity curve.

5 Conclusion

Changes in the resistivity can be explained by the depletion of the supersaturated matrix either by the precipitation, the enrichment of primary phases or the transformation of phases.

In alloys with high Si content (HV, LV and S) the considerable amount of precipitates appear. Their density and distribution depend on the total amount of alloying elements. Precipitates distributed in the matrix slow down the recovery and recrystallization.

In alloys with low Si content (Z), only few precipitates on the subgrain boundaries are created. Due to the low Si content phase transformation from metastable α-Al_8Fe_2Si through α-$Al_{15}(Mn, Fe)_3Si_2$ to $Al_6(Mn, Fe)$ occur with the increasing temperature of annealing.

Bibliography

[1] M. Slámová, M. Karlík, M. Cieslar, B. Chalupa, and P. Merle, Kovové materiály **40**, 389 (2002).

[2] M. Slámová, M. Karlík, M. Cieslar, B. Chalupa, and P. Merle, Kovové materiály **41**, 51 (2003).

[3] M. Slámová, P. Sláma, and M. Cieslar, Material science forum **519–521**, 365 (2006).

[4] *Teal Sheets - International Alloy Designations and Chemical Composition Limits for Wrought Aluminum and Wrought Aluminum Alloys*, The Aluminum Association Inc., 1525 Wilson Boulevard, Arlington, 2006.

[5] B. Smola, *Elektronová mikroskopie*, volume 1 of *Experimentální metody fyziky pevných látek*, MFF UK, Praha, 1979.

[6] M. Slámová, M. Cieslar, and P. Sláma, Fyzikálně-metalurgické základy technologie výroby tenkých fólií ze slitin AW-3003 a AW-8006, Studijní zpráva 33/05 - S, VÚK Panenské Břežany s.r.o., Panenské Břežany 50, Odolena Voda, 2005.

[7] J. E. Hatch, editor, *Aluminum: Propeties and Physical Metalurgy*, American Society for Metals, Metals Park, Ohio, 1984.